Advances in Water Resources 212 (2026) 105303

Contents lists available at ScienceDirect

Advances in Water Resources

journal homepage: www.elsevier.com/locate/advwatres

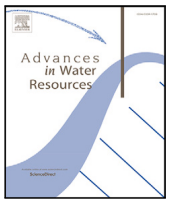

The structure of gravity currents flowing around a wall-mounted vertical circular cylinder

Giovanni Di Lollo [a], Claudia Adduce [a,*], R.M.L. Ferreira [b], A.M. Ricardo [b]

[a] Roma Tre University Department of Civil, Computer Science and Aeronautical Technologies Engineering, Via Vito Volterra 62, Rome, 00146, Italy
[b] CERIS, Instituto Superior Técnico, Universidade de Lisboa, Av. Rovisco Pais, Lisbon, 1049-001, Portugal

ARTICLE INFO

Keywords:
Gravity currents
Lock release
Vertical cylinder
PIV
Rortex
Laboratory experiments

ABSTRACT

We analyze the structure of lock-release gravity currents as they approach and flow around a vertical obstacle. Two laboratory setups are used: an undisturbed horizontal channel and the same channel partially obstructed by a circular cylinder. Instantaneous two-dimensional velocity fields were acquired with Particle Image Velocimetry. The structure of the flow is discussed in terms of its instantaneous velocity components and by identifying its characteristic vortical coherent structures employing the Rortex/Liutex vector. The current is divided in three layers, characterized by different vortical structures. The lowermost layer features the hairpin-like vortical structures of smooth boundary layers while the shear layer features the growth of inflectional instabilities. Once the head has passed, the body of the current is upwelled, disrupting the shear layer and creating a region of intense mixing. A complex vortex system is formed with rotation compatible with returning the upwelled flow back to the current. The interaction of this region with the separated ambient flow requires the formation of a horizontal vortex that compatibilizes both flows. In the ambient fluid, the observed rotational structures may be the cores of Von Kármán vortices whose axis (vertical when shed) were rotated by the upwelling current.

1. Introduction

Gravity currents are flows generated by the density gradient between two or more fluids in contact. These flows can have an important impact on the surrounding environment: temperature or salinity gradients can trigger the movement of water masses in the oceans; the release of pollutants into the atmosphere, lakes or oceans often occurs through the generation of gravity currents or plumes (Simpson, 1999).

In the last decades, several studies were devoted to the investigation of the main characteristics and dynamics of gravity currents. The propagation of gravity currents on a horizontal smooth bottom was investigated both by laboratory experiments and numerical simulations (Benjamin, 1968; Huppert and Simpson, 1980; Huppert, 1982; Hacker et al., 1996; Shin et al., 2004; Marino et al., 2005; Zhu et al., 2006; Adduce et al., 2012; Inghilesi et al., 2018; Kyrousi et al., 2018; Lombardi et al., 2018; Zordan et al., 2018a,b; Dai and Huang, 2024). During their paths, gravity currents can interact with a complex bottom boundary. Many studies investigated the influence of different bottom slopes (Cuthbertson et al., 2014; Laanearu et al., 2014; Negretti et al., 2017; Ottolenghi et al., 2017; Martin et al., 2019; De Falco et al., 2020, 2021; Dai and Huang, 2020, 2021; M. Maggi et al., 2023) or the presence of bottom roughness (La Rocca et al., 2008; Tokyay et al., 2011; Nogueira et al., 2013, 2014; Bhaganagar and Pillalamarri, 2017; He et al., 2022; Maggi et al., 2022; M. Maggi et al., 2025; M.R. Maggi et al., 2025) on the dynamics of density currents. In general, these studies show a reduction of the propagation velocity of the front, compared to the undisturbed case.

Furthermore, gravity currents can interact with a variety of obstacles, both natural and human made. The influence of artificial structures on the dynamics of gravity currents has been studied using submerged obstacles occupying the entire width of the domain, of different shapes, including triangular (Lane-Serff et al., 1995; Adduce et al., 2022; M. De Falco et al., 2021; M.R. Maggi et al., 2023; Maggi and Adduce, 2025), cylindrical (Gonzalez-Juez et al., 2009, 2010; La Rocca et al., 2013) and trapezoidal (Cuthbertson et al., 2018; Laanearu and Cuthbertson, 2023) obstacles. These works emphasize a slowdown in the propagation of current fronts due to drag and viscous forces, as the current interacts with the obstacle, enhanced the formation of complex three-dimensional separation patterns.

The interaction between density currents and emergent rigid vegetation or human-made structures can be studied using vertically mounted cylinders (Tanino et al., 2005; Zhang and Nepf, 2008; Ho and Lin,

* Corresponding author.
E-mail address: claudia.adduce@uniroma3.it (C. Adduce).

https://doi.org/10.1016/j.advwatres.2026.105303
Received 19 December 2025; Received in revised form 14 February 2026; Accepted 9 April 2026
Available online 14 April 2026

2015; Testik and Ungarish, 2016; Gu et al., 2018; Zhou and Venayagamoorthy, 2020). The passage of a gravity current within an array of cylindrical obstacles induces the transition from an inertial regime to a drag-dominated regime, resulting in the reduction of the front velocity and the total discharge rate. The drag dominated regime induces a change in the classical semi-elliptical shape of the current head, which takes on a triangular form.

Only recently the interaction of a gravity current with an isolated vertical obstacle has received attention (Mok et al., 2011; Brito et al., 2022; Di Lollo et al., 2024). Mok et al. (2011) used the laser-induced fluorescence (LIF) technique to analyze the interaction between a gravity current and an emergent vertical cylinder. Three phases have been identified: an impact phase, a transition phase, and a quasi-steady phase. An area of circulation is generated upstream of the obstruction as the result of the interaction between the rising dense current and the return flow of ambient fluid. Di Lollo et al. (2024) used Particle Image Velocimetry (PIV) technique to study the mean velocity field and the turbulence of a gravity current interacting with a emergent vertical cylinder before impact. The presence of a vertical obstacle does not significantly affect the mean velocity field but alters the redistribution mechanism of Turbulent Kinetic Energy (hereinafter TKE), reducing the intensity of TKE and Reynolds stresses within the head of a gravity current. Brito et al. (2022) validated a LES model with velocity and density measurements in the same configurations of Di Lollo et al. (2024).

This study aims to investigate how the presence of localized vertical obstacles (vegetation and/or vertical human structures) modifies the velocity field, reorganizes the flow structure and influences the formation and development of turbulent structures of a gravity current, a topic not yet addressed in the literature. The study is conducted using the simplest representation of an obstacle that does not occupy the entire width of the domain, a single vertical cylinder, as a starting point for future studies. The interaction between gravity currents and the obstacle is studied by means of instantaneous velocity measurements obtained with PIV, focusing on the phases of interaction and the visualization of vortex structures, comparing the scenario with the obstacle and the case without it, herein referred as undisturbed configuration.

In recent years, different methods for the identification and visualization of vortex structures and their evolution have been developed, such as Δ-criterion (Chong et al., 1990), Q-criterion (Hunt et al., 1988), λ_{ci}-criterion (Berdahl and Thompson, 1993; Zhou et al., 1999), $\lambda_{cr}/\lambda_{ci}$ -criterion (Chakraborty et al., 2005) and λ_{ω} -criterion (Elsas and Moriconi, 2017). Swirling strength was used to investigate the formation of vortex structures in a bottom gravity current on horizontal bed using DNS simulations, showing a complex presence of structures throughout the development of the current (Cantero et al., 2008). The influence of a seabed macro-roughness on the formation of interface vortices and on the bottom in gravity currents was analyzed instead by the Okubo–Weiss parameter, starting from two-dimensional PIV measurements in Maggi et al. (2022). These methods require the introduction of threshold values to identify vortical regions, which may lead to ambiguities, particularly in flows characterized by strong shear and strain An innovative vortex identification and visualization method, Rortex (or Liutex), is applied in this study. This method is based on the definition of a vortex vector (Rortex) which describes the local rotation of the fluid (Liu et al., 2018; Tian et al., 2018). Its direction indicates the local axis of rotation while its magnitude is defined as the rotational part of the vorticity in the direction of the vortex vector. Regions where the intensity of the vector vortex is different from zero represent the presence of a vortex.

The Rortex method has been applied and validated with several turbulent cases and compared with other methods of vortex identification (Gao and Liu, 2018; Zhan et al., 2019). The advantages of the Rortex are particularly evident in three-dimensional flows. In such configurations, vorticity does not generally coincide with the local axis of rigid-body rotation and may be strongly influenced by shear contributions. Scalar and eigenvalue-based vortex identification criteria can identify regions contaminated by shear contributions, do not provide information on the orientation of the vortex axis and may be sensitive to the choice of threshold values. By contrast, Rortex method directly identifies both the intensity and the direction of the local rotation axis, showing excellent results due to the simple calculation, the decontamination by shear contributions and the no need to define a thresholds (Gao and Liu, 2018; Dong et al., 2019; Gui et al., 2019; Liu et al., 2019; W. Xu et al., 2019; W.q. Xu et al., 2019; Zhan et al., 2019; Shrestha et al., 2021).

In two-dimensional flows, the Rortex formulation becomes a shear-free measure of local rigid-body rotation by filtering out contributions associated with pure shear. Although the rotation axis is fixed in two-dimensional configurations, this property allows a clearer identification of vortical structures in regions characterized by strong velocity gradients, such as near-wall areas and in the vicinity of obstacles. As a result, Rortex can provide a more robust vortex identification compared to vorticity-based or eigenvalue-based criteria, even in two-dimensional flow fields (Liu et al., 2018; Gao and Liu, 2018; Xia, 2021).

In this work, the intensity of the vector Rortex R is evaluated in its 2D formulation (Xia, 2021)

$$R = \begin{cases} \beta - \alpha & \text{if } \alpha^2 - \beta^2 < 0 \text{ and } \beta > 0, \\ \beta + \alpha & \text{if } \alpha^2 - \beta^2 < 0 \text{ and } \beta < 0, \\ 0 & \text{if } \alpha^2 - \beta^2 \geq 0 \end{cases} \tag{1}$$

where α and β are evaluated as

$$\alpha = \frac{1}{2}\sqrt{(\frac{\partial W}{\partial z} - \frac{\partial U}{\partial x})^2 + (\frac{\partial W}{\partial x} + \frac{\partial U}{\partial z})^2} \tag{2}$$

$$\beta = \frac{1}{2}(\frac{\partial W}{\partial x} - \frac{\partial U}{\partial z}) \tag{3}$$

and where U is the instantaneous longitudinal velocity component and W is the instantaneous vertical velocity component.

This paper is structured as follows. After this introductory section, Section 2 presents the laboratory setup and instrumentation used in the experiments. Section 3 characterizes the gravity current's layers, which will be analyzed in Sections 4 and 5 for undisturbed configuration and cylinder configuration respectively. Section 6 discusses the results observed and Section 7 summarizes the main conclusions.

2. Laboratory experiments

In this work all the gravity currents were generated by the full lock release technique in a horizontal channel with transparent walls, with a length of 3 m, height of 0.4 m, and width of 0.175 m. The setup is the same as in Di Lollo et al. (2024). A gate positioned at a distance $x_0 = 0.3$ m from the left wall of the channel temporarily separates the channel into two volumes. The left part of the channel is filled with saltwater, while the other part is filled with the ambient fluid, a mixture of water and alcohol. The fluid's depth is equal to $h_0 = 0.2$ m in both compartments. The gate removal causes the dense fluid to collapse, propagating along the bottom of the channel, underneath the ambient fluid, towards the right wall. The ambient fluid propagates in the opposite direction, generating a stratified environment with intense mixing at the interface. Two density gradients are tested, varying the amount of salt and alcohol to obtain two different reduced gravities: $g' = 0.06$ m/s^2 and $g' = 0.24$ m/s^2. The reduced gravity g' is defined as

$$g' = g\frac{\rho_1 - \rho_0}{\rho_0} \tag{4}$$

where $g = 9.81$ m/s^2 is the acceleration of gravity, ρ_1 is the density of the dense fluid and ρ_0 is the density of the ambient fluid. The density currents were tested in the free channel, here referred as undisturbed configuration, and in a setup with an emergent PVC cylinder with diameter $\phi_c = 2.5$ cm, referred as obstructed configuration. The cylinder

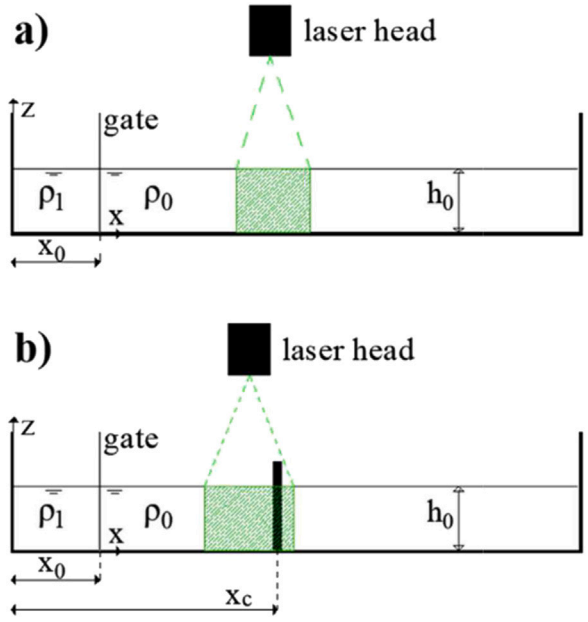

Fig. 1. Sketch of the channel lateral view for (a) undisturbed configuration and (b) obstructed configuration. The green shaded area represents the PIV field of view.

is placed at a distance of $x_c = 90$ cm from the left wall of the channel and is mounted half the width of the channel perpendicular to the bottom. Two-dimensional instantaneous velocity fields are measured by using a Dantec © 2D PIV system with a power source able to generate a pulse of 30 mJ. The laser head is positioned above the channel, directing the laser beam to illuminate a vertical plane (x, y) along the channel centerline upstream of the obstacle. In the undisturbed configuration, the PIV measurement window extends from $x = 75$ cm to $x = 100$ cm. In the configuration with the cylinder, the measurement window extends from $x = 65$ cm to $x = 95$ cm. Fig. 1 shows the experimental setup of the two configurations.

The time between laser pulses (TBP) is set equal to 12000 μs for tests with $g' = 0.06$ m/s^2, and 4500 μs for the $g' = 0.24$ m/s^2 tests. An 8-bit CCD camera with a resolution of 1200 × 1600 pixels, oriented perpendicular to the laser sheet plane, records the measurement window at an acquisition rate of 15 Hz. The synchronization between the beginning of the PIV data acquisition and the lock release is guaranteed by a switch connected to the gate. DynamicStudio, software owned by Dantec, is used to image acquisition and to compute velocity fields, applying an adaptive correlation algorithm with a final space resolution of 16 × 16 pixels and a 50 % overlap of the interrogation area, validated by a process based on the median of the 8 adjacent vectors. Flow tracers consist of polyamide particles with a density of 1.03 g/cm^3 and a mean diameter of 50 μm.

The concentrations of salt and alcohol are adjusted to match the refractive index in both mixtures, a condition necessary to avoid measurement errors when employing the PIV technique in stratified environments. The solute concentrations are determined following the procedure described by Daviero et al. (2001). Digital thermometers are used to ensure that both mixtures are at the same temperature. For further details, see Di Lollo et al. (2024). The Reynolds number for tests in the undisturbed configuration, Re, is calculated using the water depth as the characteristic length scale, while the Reynolds number in the obstructed configuration, Re_c, is based on cylinder diameter, as follows

$$Re = \frac{u_b h_0}{\nu} \tag{5}$$

$$Re_c = \frac{u_b \phi_c}{\nu} \tag{6}$$

where $u_b = \sqrt{g' h_0}$ is the buoyancy velocity and ν is the kinematic viscosity of the ambient fluid. The values obtained are $Re = 2.2 \times 10^4$ and $Re_c = 2.7 \times 10^3$ for $g' = 0.06$ m/s^2, and $Re = 4.4 \times 10^4$ and $Rec = 5.5 \times 10^3$ for $g' = 0.24$ m/s^2. Hereinafter, the asterisked variables (*) refer to dimensionless quantities. The following scales are adopted: x_0 as horizontal length scale, h_0 as vertical length scale and u_b as velocity scale. The non dimensional longitudinal coordinate is defined as $x^* = (x - x_0)/(x_0)$, while the non dimensional vertical coordinate is defined as $z^* = z/h_0$.

The dimensionless time t^* is defined as $t^* = t/(x_0/u_b)$, being $t = 0$ the instant of the gate removal.

For this reference frame, the current flow is generally positive in the longitudinal direction. Thus, we use the term "front face of the cylinder" to designate the half-surface of the cylinder facing back against the dominant longitudinal motion of the current and "in front of the cylinder" to indicate the flow region upstream but in the near vicinity of the cylinder, relatively to the dominant longitudinal motion of the current. A negative flow is that running counter the x-direction. The ambient fluid mostly runs in the negative direction. Interaction with the cylinder generates, as discussed below, regions of ambient fluid with positive motion and mixed flow with negative motion. In particular, we identify a region with separated flow, mostly of ambient fluid, whose direction is positive (and thus counter the main motion of the ambient fluid), adjacent to the front face of the cylinder. Rotations, in this reference frame, are positive if counterclockwise and negative if clockwise.

3. Current profile

The gravity currents generated by the lock-release technique are generally divided into three parts (Ooi et al., 2009; Dai, 2013; Ottolenghi et al., 2018; Zordan et al., 2018a): the leading part, or head, which forces the rise of the ambient fluid along its front; the body, characterized by large longitudinal velocity values and interface instabilities (Kelvin–Helmholtz billows); the tail, characterized by a lower height and reduced longitudinal velocity values. The current head is defined as the parts that extends from the tipping point, also called the nose, to the first billow along the fluid–fluid interface, following the procedure described in Di Lollo et al. (2024).

The current front is identified by applying the condition $\partial W^*/\partial x^* \sim 0$ while the upper interface between dense fluid and ambient fluid is identified through the condition $U^* \sim 0$ (M.C. De Falco et al., 2021; Maggi et al., 2022). The undisturbed current propagation is shown in Fig. 2, showing the space/time evolution of the dimensionless current's height, $H^* = h_c/h_0$, where h_c is the current height defined as the distance between the bottom and the interface between dense and ambient fluid. The passage of the head is characterized by increasing height values, with maximum values of $H^* \sim 0.5$, marking the transition to the current body. The transition between the body and the tail is identified by the height decrease over time. The interaction between a gravity current and a vertically mounted cylinder develops in three time phases, as reported by Mok et al. (2011). The first stage is the impact, in which an initial increase of the dense current height occurs in the vicinity of the obstacle. Then, the second phase corresponds to the interaction of the cylinder with the dense current flowing in one direction and the ambient fluid flowing on the opposite direction. The maximum current height is observed in this second phase reaching $H^* = 0.7$ as reported by Mok et al. (2011). The final phase corresponds to the decrease of the dense current's height. Fig. 2(b) shows the space–time evolution of the current's dimensionless height in the configuration with the cylinder.

Gravity currents are, often, divided into two layers (Kneller et al., 1999; Cossu and Wells, 2012; Kashefipour et al., 2018). We, nevertheless, and for the sake of our arguments, opt for a different description

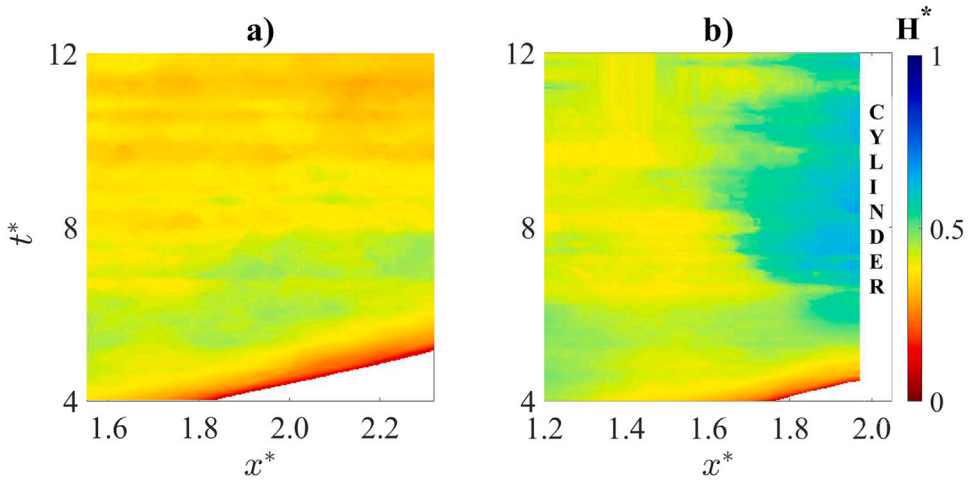

Fig. 2. Space-time map of the dimensionless height of the current in (a) the undisturbed configuration and (b) the obstructed configuration, for tests with $g' = 0.06$ m/s^2.

of the flow, proposing a stratification with 3 non-overlapping layers: a lowermost layer (herein inner layer), whose dynamics is essentially determined by the interaction of the current with the smooth wall below; a shear layer between the dense fluid and the ambient fluid, where both fluids mix, where instabilities form and grow due to the strong inflectional profile, forming Kelvin–Helmotz billows that promote the aforementioned mixing; and a core layer between the previous two, herein the outer layer. An upper ambient fluid layer remains above the shear layer.

The inner layer extends from the bed up to the height of the maximum longitudinal velocity component, $U^*_{max}(x^*, t^*)$. The thickness of the shear layer $\delta^*(x^*, t^*)$ can be calculated by the following equation (Zhu and Lawrence, 2001; Pham et al., 2009; M.C. De Falco et al., 2021)

$$\delta^*(x^*, t^*) = \frac{U^*_{max,d}(x^*, t^*) - U^*_{min,a}(x^*, t^*)}{(\frac{dU^*}{dz^*})(x^*, t^*)_{max}} \tag{7}$$

where $U^*_{max,d}(x^*, t^*)$ is the maximum longitudinal velocity component of the dense fluid of each vertical profile, $U^*_{min,a}(x^*, t^*)$ is the minimum velocity component of the ambient fluid of each vertical profile and $(\frac{dU^*}{dz^*})(x^*, t^*)_{max}$ is the maximum vertical shear rate of the longitudinal velocity component. The outer layer extends from the upper boundary of the inner layer to the lower boundary of the shear layer. Fig. 3 shows the three layers.

4. Current dynamics in the undisturbed configuration

This section describes the dynamics of the gravity currents in the undisturbed conditions. It is based on the analysis of instantaneous velocity field and on the identification of rotational structures, calculated as the magnitude of the Rortex vector. The results shown refer to the $g' = 0.06$ m/s^2 test. Similar results were observed in the $g' = 0.24$ m/s^2 test.

4.1. Velocity field

Fig. 4 presents maps of $U^*(x^*, z^*, t^*)$ in the undisturbed configuration for $g' = 0.06$ m/s^2, overlapped by its vertical profile in three different positions at different time instants. The dense current is characterized by positive values of $U^*(x^*, z^*, t^*)$, while the ambient fluid is characterized by negative velocities. The shape of the vertical profile of longitudinal velocity shown in Fig. 4 is consistent with the literature (Kneller et al., 1999; Cossu and Wells, 2012). In the inner layer, the longitudinal velocity shows a positive gradient along the vertical, increasing from zero at the bottom to the maximum value at the top in a non-linear fashion. In the outer layer, there is a reversal of the velocity gradient and the longitudinal velocity decreases from the maximum value. In the shear layer, there is a transition from positive velocity values of the dense fluid to negative velocity values of the ambient fluid, separated by the zero velocity values at the interface between the two fluids. Longitudinally, the magnitude of the longitudinal velocity decreases from the head to the current tail.

Fig. 5 show maps of $W^*(x^*, z^*, t^*)$ for the undisturbed current characterized by $g' = 0.06$ m/s^2. The highest values of $W^*(x^*, z^*, t^*)$ are observed on the top of the current head, where the ambient fluid is displaced upward due to the progress of the dense current. In the current body and tail, the vertical velocity presents low magnitude in the shear layer while it is negligible elsewhere.

4.2. Rortex intensity

Fig. 6 shows the Rortex intensity, R^*, for the undisturbed configuration characterized by $g' = 0.06$ m/s^2. The inner layer is predominantly characterized by negative Rortex intensities, indicating the presence of clockwise vortices, most likely associated to the heads of hairpin vortices as in the steady flow over smooth walls. The formation of vortices has been observed at channel bottom and at the upper limit of the inner layer. The strongest intensity vortices are observed during the passage of the head and body of the current ($t^* = 4.85$ and $t^* = 5.26$ in Fig. 6), manifesting either as isolated vortices or connected structures extending between the two limits of the inner layer. During the current propagation, the vortex intensity decreases. The shear layer is characterized by intense positive rotational structures, counterclockwise vortices generated by the movement of the two fluids in opposite direction. In the upper part of the current head ($x^* = 1.8$ at $t^* = 4.85$ in Fig. 6), there is the formation of an intense positive vortex structure, which resembles the formation of Kelvin–Helmholtz billows. These structures maintain a well-defined and visible core until $t^* = 6.14$. After that time instant, a stretching process begins, which is identified by the rupture of the vortex core and the generation of sparse intense R^* signals within the shear layer. During the passage of the current body and tail, in the observation window, no additional coherent structures are observed, only isolated vortices with decreasing intensity are observed. In the initial stages of current propagation ($t^* = 4.85$ and $t^* = 5.26$ in Fig. 6), strong positive Rortex intensities are identified in the outer layer of the current head and near the lower limit of the shear layer. It seems to be a consequence of the formation of intense interface vortices. After the stretching of the interface instability discussed above, the increase of Rortex intensities was observed in the outer layer. The formation of a pronounced isolated vortex was

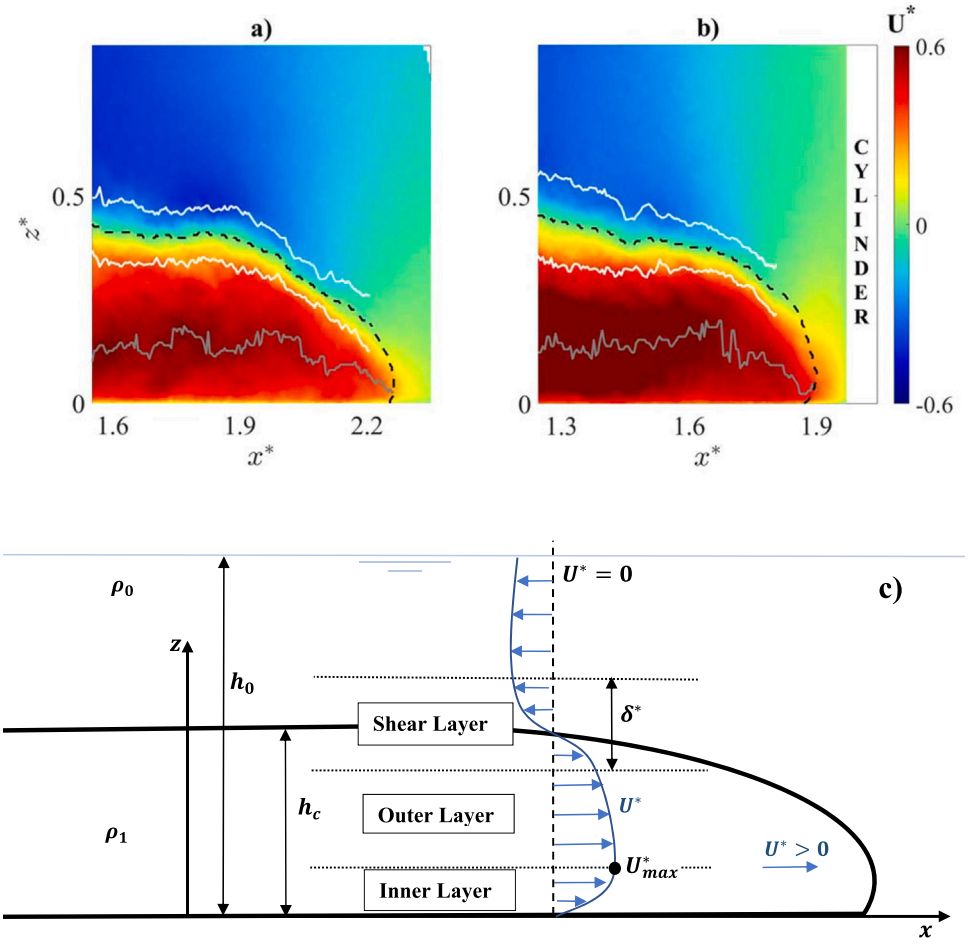

Fig. 3. Identification of the flow layers in currents in: (a) the undisturbed configuration characterized by $g' = 0.06$ m/s^2; and (b) the obstructed configuration characterized by $g' = 0.06$ m/s^2. The dashed black line is the current profile, the gray line represents the upper limit of the inner layer and the white lines delimit the shear layer. (c) Schematic of the gravity current divided into the three layers.

observed at $x^* = 1.8$ at $t^* = 6.14$, situated immediately below the lower boundary of the shear layer. As the current progresses, this vortex moves towards the inner layer, being carried by the flow and thereby intensifying its extension, probably as a result of the interaction with other vortices present in the outer layer.

The vortex structures identified herein with the Rortex method are in agreement with the results of Cantero et al. (2008), where the turbulent structures of an undisturbed gravity current simulated numerically with DNS are analyzed by the swirlingt strength. From numerical simulations, the authors highlighted the different phases of Kelvin–Helmotz billows, their formation and the maintenance of coherence during the initial stages of current propagation. In addition, Cantero et al. (2008) show that, after a stretching and tilting process, those interface vortices break up into smaller structures, generating vortices in the outer layer, where they were previously absent. Other research works have also showed that the raised clockwise vortex in the inner layer can be attributed to the head of hairpin vortices, while the bed structures represent the tail of the same vortices or the presence of other cane or horseshoe vortices, common turbulent structures present in the turbulent boundary layer (Head and Bandyopadhyay, 1981; Cantero et al., 2008; Eitel-Amor et al., 2015; Pang et al., 2023). It is interesting to note how the evolution of the inner layer tends to change due to these clockwise vortices. The changes in height of the inner layer can be attributed to the higher velocities found in the presence of the hairpin vortex head (Theodorsen, 1955; Adrian, 2007).

5. Dynamics of current/obstacle interaction

This section describes the interaction of the dense current and of the ambient fluid with the cylinder. The results shown are relative to the current characterized by $g' = 0.06$ m/s^2, as no significant differences were observed in the configuration with $g' = 0.24$ m/s^2.

5.1. Velocity field

Fig. 7 shows maps of $U^*(x^*, z^*, t^*)$ in the obstructed configuration for $g' = 0.06$ m/s^2 overlapped by vertical profiles at three different positions and different time instants. Before the impact with the cylinder, no significant variations have been identified in the longitudinal velocity of the current when compared to the undisturbed current ($t^* = 3.49$ in Fig. 7). A Reynolds number for the ambient fluid upstream of the cylinder Re_{amb} is evaluated as

$$Re_{amb} = \frac{\bar{U}_{amb}\phi_c}{\nu} \tag{8}$$

where $\bar{U}_{amb}$ is the mean ambient fluid velocity, evaluated for each time t. Re_{amb} reaches values up to 900. These values are higher than the critical threshold required for the formation of a von Kármán vortex street downstream of a cylindrical obstacle (Jackson, 1987; Wiliamson, 1996). It can therefore be stated that the passage of the ambient fluid generates a von Kármán vortex street upstream of the cylinder, with vortices being transported in the negative direction in the ambient fluid flow.

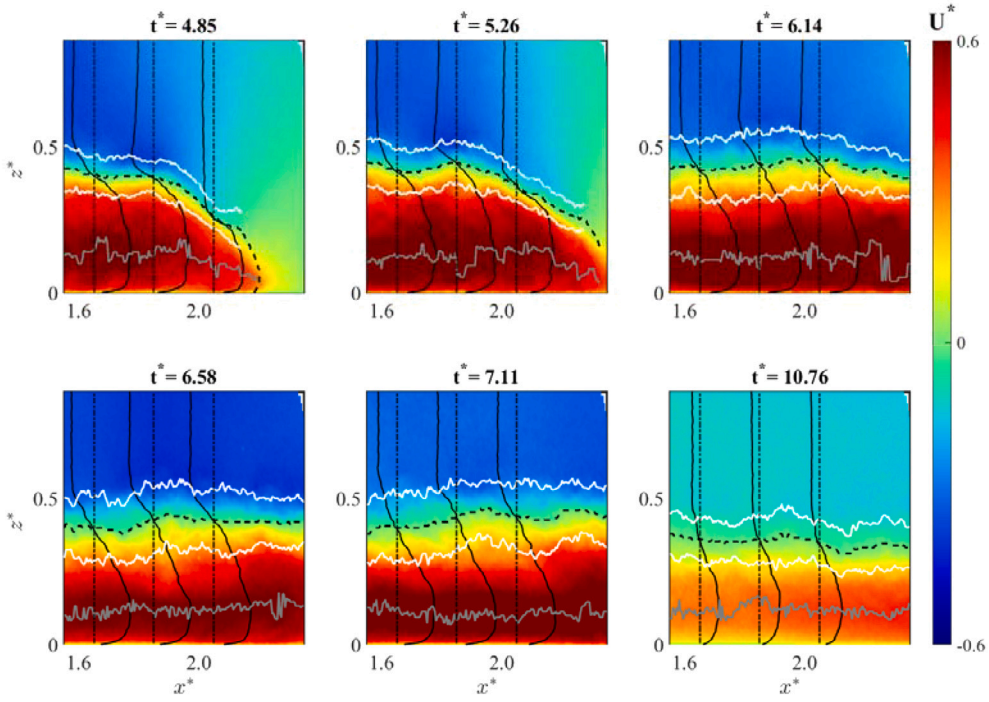

Fig. 4. Maps of instantaneous longitudinal velocity component in the undisturbed configuration for $g' = 0.06$ m/s^2 with vertical profile at three positions: $x^* = 1.65$, $x^* = 1.85$ and $x^* = 2.05$. The dashed black line is the current profile, the gray line represents the upper limit of the inner layer and the white lines delimit the shear layer.

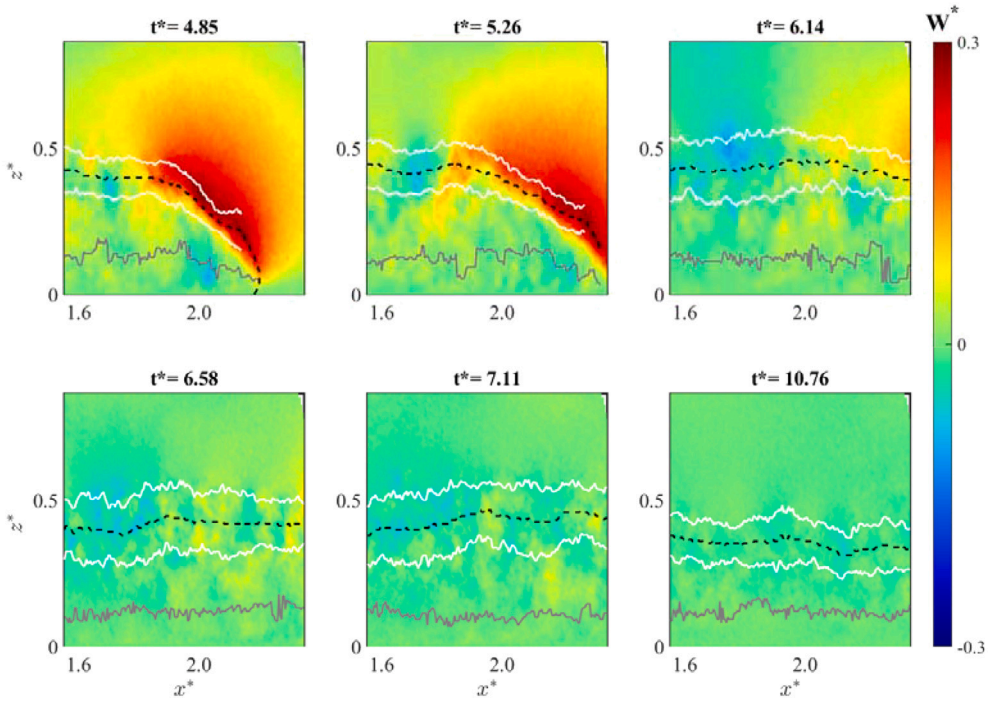

Fig. 5. Maps of instantaneous vertical velocity component in the undisturbed configuration for $g' = 0.06$ m/s^2. The dashed black line is the current profile, the gray line represents the upper limit of the inner layer and the white lines delimit the shear layer.

After the impact, part of the current flows around the obstacle, while another upwells in front of the cylinder and the current longitudinal velocity decreases ($t^* = 5.34$ in Fig. 7). Eventually, the upwelled flow mixes with the ambient fluid and is transported back into the current in the negative longitudinal and vertical directions. As the current body propagates around the cylinder and upwells in front of it,

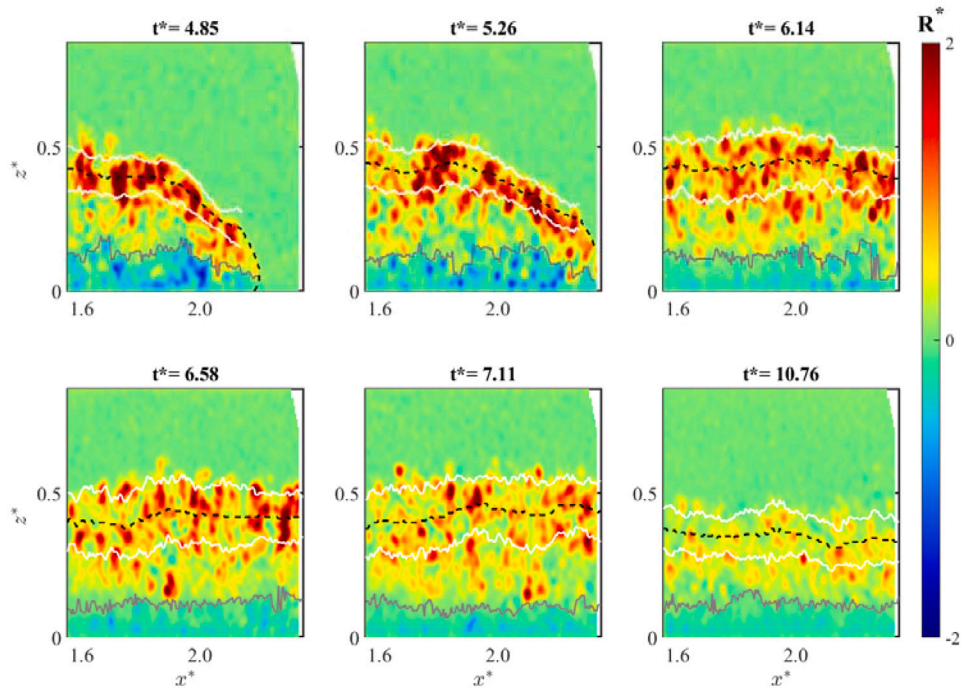

Fig. 6. Maps of the Rortex intensity, R^*, in the undisturbed configuration for $g' = 0.06$ m/s^2 . The dashed black line is the current profile, the gray line represents the upper limit of the inner layer and the white lines delimit the shear layer.

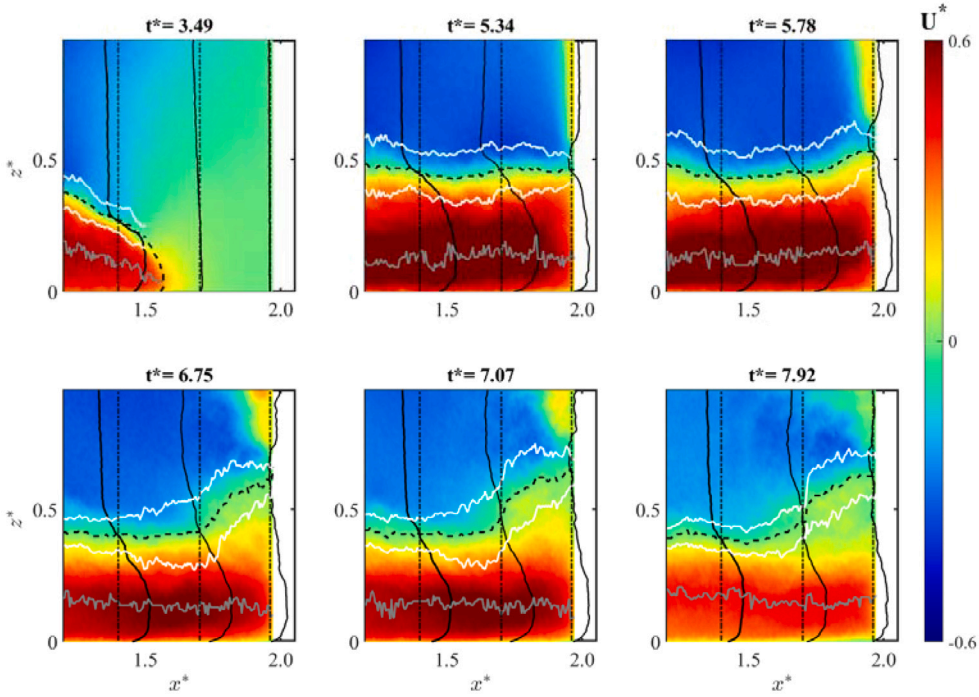

Fig. 7. Maps of longitudinal velocity, $U^*(x^*, z^*, t^*)$, in obstructed configuration for $g' = 0.06$ m/s^2 with vertical profiles at $x^* = 1.45$, $x^* = 1.75$ and $x^* = 1.95$. The dashed black line is the current profile, the gray line represents the upper limit of the inner layer and the white lines delimit the shear layer.

the ambient fluid moves in the opposite direction ($t^* = 5.34$ in Fig. 7). It eventually forms a strong separation region adjacent to the front face of the cylinder. Hereinafter, this region is designated by recirculation zone as it corresponds to the region where the ambient fluid is entrapped and redirected towards the obstacle, the opposite direction of the general ambient fluid movement.

As the dense fluid moves upward in front of the obstacle, the area available for the passage of ambient fluid decreases and the recirculation zone undergoes a decrease in vertical extent and an increase in width ($t^* = 5.78$ and $t^* = 6.75$ in Fig. 7). At the same time, longitudinal velocities increase within the recirculation zone close to the free surface. Close to the obstacle, the shear layer is disrupted and

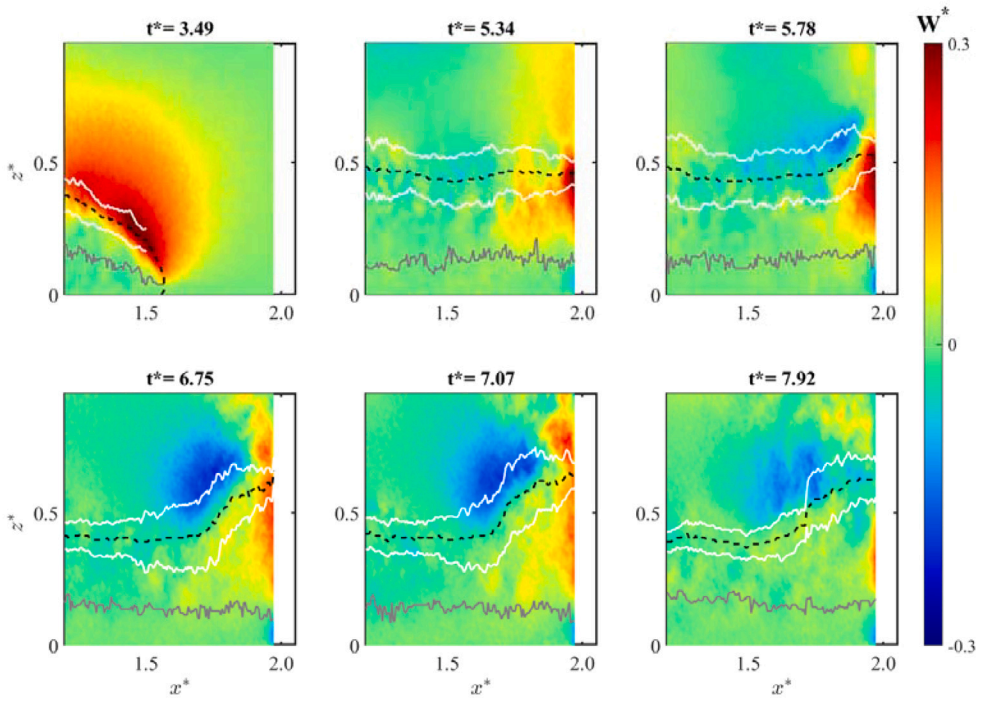

Fig. 8. Maps of vertical velocity, $W^*(x^*, z^*, t^*)$, in the configuration with the cylinder for $g' = 0.06$ m/s^2. The dashed black line is the current profile, the gray line represents the upper limit of the inner layer and the white lines delimit the shear layer.

the flow exhibits nearly zero longitudinal velocity magnitudes, while far from the cylinder (i.e. $x^* = 1.4$), the behavior is the same observed in the undisturbed configuration.

Fig. 8 shows maps of $W^*(x^*, z^*, t^*)$. Before the impact, the highest values of vertical velocity are concentrated on the top of the current head, whilst negligible values are exhibited in the inner and outer layers, similarly to the undisturbed configuration ($t^* = 3.49$ in Fig. 8). After the impact, positive values of the vertical velocity component are observed in the outer layer and in the shear layer, with maximum values observed on the vicinity of the obstacle ($t^* = 5.78$ in Fig. 8). After the upwelling of the current, positive values are also observed in the recirculation zone. Upstream of the upwelling, there are strong negative values of vertical velocity, indicating vertical downward motion of ambient fluid towards the dense current ($t^* = 6.75$ and $t^* = 7.07$ in Fig. 8). The inner layer shows negative values of vertical velocity in the vicinity of the obstacle, indicating that near the lower part of the obstacle there is flow moving downwards to cross the obstacle from the sides. Far from the cylinder, the inner layer has no vertical motion.

5.2. Rortex intensity

Fig. 9 shows R^* for $g' = 0.06$ m/s^2. The Rortex intensity maps show that, before the impact, the vortex distribution is similar that observed in the undisturbed condition ($t^* = 3.49$ in Fig. 9). The inner layer is characterized by clockwise rotations, while the maximum positive values of R^* are identified in the shear layer, due to the movement in opposite direction of the two fluids. An intense persistent, negative-intensity vortex form in the inner layer after the impact ($t^* = 5.34$ in Fig. 9). The Rortex intensity of this vortex structure in the inner layer increases as the current propagates, while no relevant structures have been identified in this layer far from the cylinder. From $t^* = 5.78$ there is the formation of a shear region that compatibilizes the circulation flow and the flow in the separated region. There is no significant extension of this structure in the longitudinal direction, so it remains confined to the vicinity of the obstacle. After the impact, following the increase of the current height ($t^* = 6.75$ in Fig. 9), clockwise and counterclockwise vortices are generated in the recirculation zone and propagated away from the cylinder's vicinity, in the direction of the ambient fluid motion. The intensity and frequency of those vortices increase with time ($t^* = 7.07$ and $t^* = 7.92$ in Fig. 9). The outer layer is characterized by positive Rortex intensity.

6. Discussion

The interaction between a gravity current and a vertically mounted cylinder leads to the formation of intense vortex structures. The vortex structure identified in the inner layer, close to the cylinder, is similar to a horseshoe vortex, a structure observed in previous studies on the flow dynamics at the base of a vertical obstacle not occupying the total width of the domain (Baker, 1980; Dey and Raikar, 2007; Chen et al., 2019; Zhang et al., 2020).

The interaction between the rising dense fluid and the ambient fluid flowing in the opposite direction near the obstacle causes an intense counterclockwise vortex in front of the obstacle, after the impact ($t^* = 5.78$ in Fig. 9). The clockwise vortex observed above this structure is generated by the interaction between the rising dense fluid and the ambient fluid trapped in the recirculation zone. The increase of dense current height in front of the obstacle leads to a strong circulation on the upstream side. This circulation expands while the current height increases and remains with the same size during the following current descent phase. After the impact, the dense current shows no significant reflection in front of the obstacle, only an increase in the current height is observed. A similar result was obtained by Brito et al. (2022), based on measurements of the density field in the same setup. This suggests that the strong rotation, identified herein employing the Rortex method, contributes to increase the mixing between the two fluids. The downward flow that is observed above the interface, resulting from the current-obstacle impact, is not only reflected dense fluid, but a mixture of dense and ambient fluids characterized by a lower density than that of the current. This observation explains the unchanged concentration profile obtained in the work of Brito et al. (2022).

Less clear is the formation of vortices in the recirculation zone. Two hypotheses are proposed:

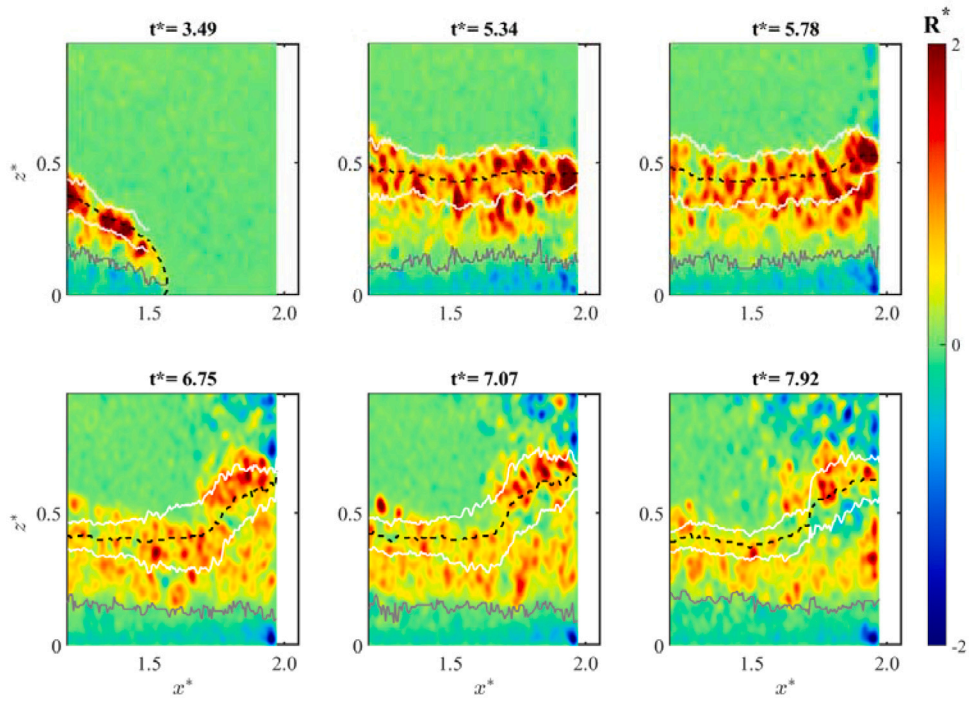

Fig. 9. Maps of Rortex intensity in the obstructed configuration for $g' = 0.06$ m/s^2. The dashed black line is the current profile, the gray line represents the upper limit of the inner layer and the white lines delimit the shear layer.

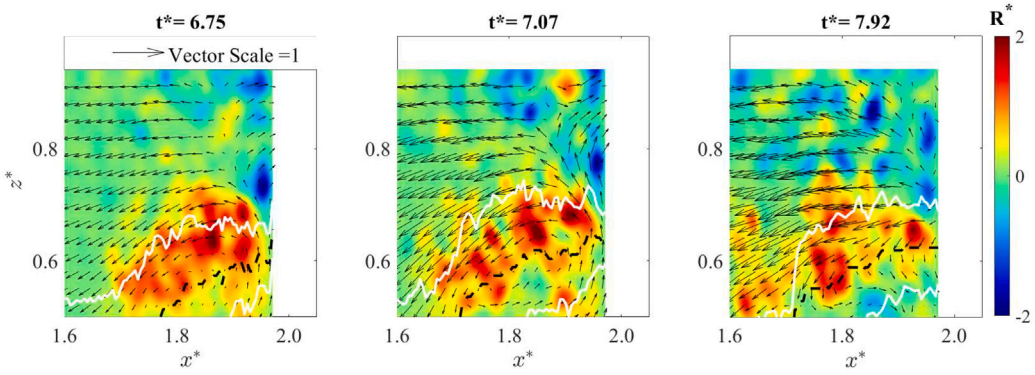

Fig. 10. Maps of Rortex intensity in the obstructed configuration for $g' = 0.06$ m/s^2 in the recirculation zone. The quiver maps represent the non dimensional velocity field. The dashed black line is the current profile and the white lines delimit the shear layer.

- *tilting mechanism*: the rising dense fluid would impact the vortices generated in the Von Kármán street of the cylinder, tilting them and generating clockwise rotations with the axis of rotation perpendicular to the (x,y) plane, visible in the configuration of the present work when the vortices cross the PIV laser beam. This hypothesis could explain the formation of clockwise vortices in the initial phases near the cylinder, not the presence of counterclockwise vortices.
- *Alternating flow propagation*: in the recirculation zone there is an alternation of vertical movements of opposite sign, as shown by the velocity field in Fig. 10. For $t^* = 6.75$ there are vertical movements directed upwards and converging towards the cylinder; at $t^* = 7.07$ a downward flow from the free surface is observed in which one part converges towards the cylinder while the other propagates upstream; for $t^* = 7.92$ vertical downward flow movements are found near the surface of the cylinder, with opposite direction relatively to the vertical movements identified further upstream. There is, therefore, propagation of the fluid mass in different directions, probably enough for the formation of vortices rotating in opposite directions.

The results obtained in this study allow us to draw some implications regarding the interaction of gravity currents with vegetation and/or vertical human structures. The presence of a single cylinder causes dense currents to accumulate along its surface, resulting in the formation of a vortex upstream of the obstacle. This structure could reduce the transport of sediments and/or pollutants by a gravity current downstream of a vegetated area. Particles and debris could become trapped in the vortex formed upstream of the vegetation, remaining suspended until the tail of the current passes. Subsequently, they would be drawn into a slower flow, favoring their sedimentation upstream of the vegetation. The intensity of the vortices in the inner region in the configuration with the cylinder are less intense than in the undisturbed case, which is in line with the reduction of turbulence in a gravity currents approaching a vertical cylinder found in Di Lollo et al. (2024). This leads to a possible decrease in the remobilization of sedimented particles and increases the concentration of

sediment upstream of the vegetation compared to a case without vegetation. The passage of a gravity current can cause erosion at the base of a vertical human-made structure as a result of the formation of an intense, persistent vortex structure, observed at the base of the cylinder.

7. Conclusions

This work researches the vortex structures of a gravity current generated by the lock-release technique through an innovative visualization method, the Rortex Liutex method. The study covers the analysis of the formation and development of vortex structures in the cases of an undisturbed current and a current impacted by the presence of a cylinder mounted perpendicular to the channel bottom. Instantaneous velocity fields were acquired by a 2D-2C PIV system on the vicinity of the cylinder.

The structures identified in the undisturbed configuration using the Rortex method are consistent with observations from previous studies.

Intense vortex structures are identified at the interface between the two fluids, as well as on the channel bottom, with the formation of packages of structures also observed in turbulent boundary layer flows. The interface structures follow stages of generation, formation, stretching, and rupture.

After the impact with the obstacle, an intense vortex is generated in the vicinity of the obstacle, caused by the rising current interacting with the ambient fluid flowing around the obstacle. This structure leads to an increase in mixing between the two fluids and could increase particle residence time and enhanced retention processes. In the upper part of the vicinity of the obstacle, the updraft of the current causes a recirculating zone in which the ambient fluid is trapped. This zone is pushed towards the free surface by the rising of the current, increasing its extension and generating intense and scattered vortices. The nature of these vortices was not possible to confirm in this work, however it is suggested that it may be due to a tilting of the vortices generated by the passage of the ambient fluid as well as on the alternation of the direction of the flow upstream of the cylinder. The reduction in the intensity of the vortices within the inner region of the current may limit sediment mobilization and resuspension. At the foot of the obstacle there is the generation of an intense clockwise vortex which may enhance localized erosion processes.

CRediT authorship contribution statement

Giovanni Di Lollo: Writing – review & editing, Writing – original draft, Software, Methodology, Investigation, Formal analysis, Data curation. **Claudia Adduce:** Writing – review & editing, Supervision, Resources, Funding acquisition. **R.M.L. Ferreira:** Writing – review & editing, Supervision, Resources, Methodology, Conceptualization. **A.M. Ricardo:** Writing – review & editing, Supervision, Methodology, Funding acquisition, Conceptualization.

Declaration of competing interest

The authors declare that they have no known competing financial interests or personal relationships that could have appeared to influence the work reported in this paper.

Acknowledgments

This work was partially supported by Foundation for Science and Technology, Portugal through funding UID/06438/2025 of the research unit CERIS (DOI:10.54499/UID/06438/2025) and through the research project DT4Rivers 2023.18404.ICD / COMPETE2030-FEDER-00760800.

This research was funded by European Union - Next Generation EU, Mission 4, Component 1 CUP F53D23001910006.

Data availability

Data will be made available on request.

References

Adduce, C., Maggi, M.R., De Falco, M.C., 2022. Non-intrusive density measurements in gravity currents interacting with an obstacle. Acta Geophys. 1–12.
Adduce, C., Sciortino, G., Proietti, S., 2012. Gravity currents produced by lock exchanges: experiments and simulations with a two-layer shallow-water model with entrainment. J. Hydraul. Eng. 138 (2), 111–121.
Adrian, R.J., 2007. Hairpin vortex organization in wall turbulence. Phys. Fluids 19 (4).
Baker, C., 1980. The turbulent horseshoe vortex. J. Wind Eng. Ind. Aerodyn. 6 (1–2), 9–23.
Benjamin, T.B., 1968. Gravity currents and related phenomena. J. Fluid Mech. 31 (2), 209–248.
Berdahl, C., Thompson, D., 1993. Eduction of swirling structure using the velocity gradient tensor. AIAA J. 31 (1), 97–103.
Bhaganagar, K., Pillalamarri, N.R., 2017. Lock-exchange release density currents over three-dimensional regular roughness elements. J. Fluid Mech. 832, 793–824.
Brito, M., Ferreira, R., Sousa, A., Farias, R., Di Lollo, G., Ricardo, A., Gil, L., 2022. LES validation of lock-exchange density currents interacting with an emergent bluff obstacle. Environ. Fluid Mech. 1–25.
Cantero, M.I., Balachandar, S., García, M.H., Bock, D., 2008. Turbulent structures in planar gravity currents and their influence on the flow dynamics. J. Geophys. Res.: Ocean. 113 (C8).
Chakraborty, P., Balachandar, S., Adrian, R.J., 2005. On the relationships between local vortex identification schemes. J. Fluid Mech. 535, 189–214.
Chen, Q., Yang, Z., Wu, H., 2019. Evolution of turbulent horseshoe vortex system in front of a vertical circular cylinder in open channel. Water 11 (10), 2079.
Chong, M.S., Perry, A.E., Cantwell, B.J., 1990. A general classification of three-dimensional flow fields. Phys. Fluids A: Fluid Dyn. 2 (5), 765–777.
Cossu, R., Wells, M.G., 2012. A comparison of the shear stress distribution in the bottom boundary layer of experimental density and turbidity currents. Eur. J. Mech. B Fluids 32, 70–79.
Cuthbertson, A., Laanearu, J., Carr, M., Sommeria, J., Viboud, S., 2018. Blockage of saline intrusions in restricted, two-layer exchange flows across a submerged sill obstruction. Environ. Fluid Mech. 18 (1), 27–57.
Cuthbertson, A., Lundberg, P., Davies, P., Laanearu, J., 2014. Gravity currents in rotating, wedge-shaped, adverse channels. Environ. Fluid Mech. 14, 1251–1273.
Dai, A., 2013. Experiments on gravity currents propagating on different bottom slopes. J. Fluid Mech. 731, 117–141.
Dai, A., Huang, Y.L., 2020. Experiments on gravity currents propagating on unbounded uniform slopes. Environ. Fluid Mech. 20 (6), 1637–1662.
Dai, A., Huang, Y.L., 2021. Boussinesq and non-Boussinesq gravity currents propagating on unbounded uniform slopes in the deceleration phase. J. Fluid Mech. 917, A23.
Dai, A., Huang, Y.L., 2024. The flow within the head of a gravity current. J. Fluid Mech. 997, A42.
Daviero, G., Roberts, P., Maile, K., 2001. Refractive index matching in large-scale stratified experiments. Exp. Fluids 31 (2), 119–126.
De Falco, M.C., Adduce, C., Cuthbertson, A., Negretti, M.E., Laanearu, J., Malcangio, D., Sommeria, J., 2021. Experimental study of uni-and bi-directional exchange flows in a large-scale rotating trapezoidal channel. Phys. Fluids 33 (3).
De Falco, M., Adduce, C., Maggi, M., 2021. Gravity currents interacting with a bottom triangular obstacle and implications on entrainment. Adv. Water Resour. 154, 103967.
De Falco, M., Adduce, C., Negretti, M., Hopfinger, E., 2021. On the dynamics of quasi-steady gravity currents flowing up a slope. Adv. Water Resour. 147, 103791.
De Falco, M., Ottolenghi, L., Adduce, C., 2020. Dynamics of gravity currents flowing up a slope and implications for entrainment. J. Hydraul. Eng. 146 (4), 04020011.
Dey, S., Raikar, R.V., 2007. Characteristics of horseshoe vortex in developing scour holes at piers. J. Hydraul. Eng. 133 (4), 399–413.
Di Lollo, G., Adduce, C., Brito, M., Ferreira, R.M., Ricardo, A.M., 2024. Turbulent kinetic energy redistribution in a gravity current interacting with an emergent cylinder. Adv. Water Resour. 183, 104585.
Dong, X., Gao, Y., Liu, C., 2019. New normalized rortex/vortex identification method. Phys. Fluids 31 (1).
Eitel-Amor, G., Örlü, R., Schlatter, P., Flores, O., 2015. Hairpin vortices in turbulent boundary layers. Phys. Fluids 27 (2).
Elsas, J., Moriconi, L., 2017. Vortex identification from local properties of the vorticity field. Phys. Fluids 29 (1).
Gao, Y., Liu, C., 2018. Rortex and comparison with eigenvalue-based vortex identification criteria. Phys. Fluids 30 (8).
Gonzalez-Juez, E., Meiburg, E., Constantinescu, G., 2009. Gravity currents impinging on bottom-mounted square cylinders: flow fields and associated forces. J. Fluid Mech. 631, 65–102.
Gonzalez-Juez, E., Meiburg, E., Tokyay, T., Constantinescu, G., 2010. Gravity current flow past a circular cylinder: forces, wall shear stresses and implications for scour. J. Fluid Mech. 649, 69–102.

Gu, Z., Ho, H.C., Wang, Z., Lin, Y.T., 2018. Laboratory studies on nearshore density-driven exchange flow over a partly vegetated slope. Water 10 (8), 1073.
Gui, N., Qi, H.b., Ge, L., Cheng, P.x., Wu, H., Yang, X.t., Tu, J.y., Jiang, S.y., 2019. Analysis and correlation of fluid acceleration with vorticity and Liutex (Rortex) in swirling jets. J. Hydrodyn. 31 (5), 864–872.
Hacker, J., Linden, P., Dalziel, S., 1996. Mixing in lock-release gravity currents. Dyn. Atmos. Oceans 24 (1–4), 183–195.
He, Z., Han, D., Lin, Y.T., Zhu, R., Yuan, Y., Jiao, P., 2022. Propagation, mixing, and turbulence characteristics of saline and turbidity currents over rough and permeable/impermeable beds. Phys. Fluids 34 (6).
Head, M., Bandyopadhyay, P., 1981. New aspects of turbulent boundary-layer structure. J. Fluid Mech. 107, 297–338.
Ho, H.C., Lin, Y.T., 2015. Gravity currents over a rigid and emergent vegetated slope. Adv. Water Resour. 76, 72–80.
Hunt, J.C., Wray, A.A., Moin, P., 1988. Eddies, streams, and convergence zones in turbulent flows. In: Studying Turbulence Using Numerical Simulation Databases, 2. Proceedings of the 1988 Summer Program.
Huppert, H.E., 1982. The propagation of two-dimensional and axisymmetric viscous gravity currents over a rigid horizontal surface. J. Fluid Mech. 121, 43–58.
Huppert, H.E., Simpson, J.E., 1980. The slumping of gravity currents. J. Fluid Mech. 99 (4), 785–799.
Inghilesi, R., Adduce, C., Lombardi, V., Roman, F., Armenio, V., 2018. Axisymmetric three-dimensional gravity currents generated by lock exchange. J. Fluid Mech. 851, 507–544.
Jackson, C., 1987. A finite-element study of the onset of vortex shedding in flow past variously shaped bodies. J. Fluid Mech. 182, 23–45.
Kashefipour, S.M., Daryaee, M., Ghomeshi, M., 2018. Effect of bed roughness on velocity profile and water entrainment in a sedimentary density current. Can. J. Civ. Eng. 45 (1), 9–17. http://dx.doi.org/10.1139/cjce-2016-0490.
Kneller, B.C., Bennett, S.J., McCaffrey, W.D., 1999. Velocity structure, turbulence and fluid stresses in experimental gravity currents. J. Geophys. Res.: Ocean. 104 (C3), 5381–5391.
Kyrousi, F., Leonardi, A., Roman, F., Armenio, V., Zanello, F., Zordan, J., Juez, C., Falcomer, L., 2018. Large eddy simulations of sediment entrainment induced by a lock-exchange gravity current. Adv. Water Resour. 114, 102–118.
La Rocca, M., Adduce, C., Sciortino, G., Pinzon, A.B., 2008. Experimental and numerical simulation of three-dimensional gravity currents on smooth and rough bottom. Phys. Fluids 20 (10).
La Rocca, M., Prestininzi, P., Adduce, C., Sciortino, G., Hinkelmann, R., 2013. Lattice Boltzmann simulation of 3D gravity currents around obstacles. Int. J. Offshore Polar Eng. 23 (03).
Laanearu, J., Cuthbertson, A., 2023. Hydraulics of stratified sill flows within varying channel geometries: investigating energy loss and mixing of maximal two-layer exchange. Environ. Fluid Mech. 23 (2), 429–464.
Laanearu, J., Cuthbertson, A.J., Davies, P.A., 2014. Dynamics of dense gravity currents and mixing in an up-sloping and converging vee-shaped channel. J. Hydraul. Res. 52 (1), 67–80.
Lane-Serff, G., Beal, L., Hadfield, T., 1995. Gravity current flow over obstacles. J. Fluid Mech. 292, 39–53.
Liu, J., Gao, Y., Liu, C., 2019. An objective version of the rortex vector for vortex identification. Phys. Fluids 31 (6).
Liu, C., Gao, Y., Tian, S., Dong, X., 2018. Rortex—A new vortex vector definition and vorticity tensor and vector decompositions. Phys. Fluids 30 (3).
Lombardi, V., Adduce, C., La Rocca, M., 2018. Unconfined lock-exchange gravity currents with variable lock width: laboratory experiments and shallow-water simulations. J. Hydraul. Res. 56 (3), 399–411.
Maggi, M.R., Adduce, C., 2025. Laboratory experiments on reflected gravity currents and implications for mixing. Water 17 (7), 1062.
Maggi, M., Adduce, C., Lane-Serff, G., 2023. Gravity currents interacting with slopes and overhangs. Adv. Water Resour. 171, 104339.
Maggi, M.R., Adduce, C., Negretti, M.E., 2022. Lock-release gravity currents propagating over roughness elements. Environ. Fluid Mech. 1–20.
Maggi, M.R., Di Lollo, G., Adduce, C., 2025. Dynamics and mixing of gravity currents over an array of cylindrical obstacles. Phys. Fluids 37 (7).
Maggi, M., Hopfinger, E.J., Sommeria, J., Adduce, C., Viboud, S., Valran, T., Negretti, M.E., 2025. Laboratory experiments of rotating stratified exchange flows over a sediment bed. Adv. Water Resour. 200, 104959.
Maggi, M.R., Negretti, M.E., Hopfinger, E.J., Adduce, C., 2023. Turbulence characteristics and mixing properties of gravity currents over complex topography. Phys. Fluids 35 (1).
Marino, B., Thomas, L., Linden, P., 2005. The front condition for gravity currents. J. Fluid Mech. 536, 49–78.
Martin, A., Negretti, M.E., Hopfinger, E.J., 2019. Development of gravity currents on slopes under different interfacial instability conditions. J. Fluid Mech. 880, 180–208.
Mok, K.M., Leong, C.S., Hoi, K.I., Yeh, H.H., 2011. The impact of a gravity current with a vertically mounted circular cylinder: An experimental study. In: 2011 IEEE 3rd International Conference on Communication Software and Networks. IEEE, pp. 194–198.
Negretti, M.E., Flor, J.B., Hopfinger, E.J., 2017. Development of gravity currents on rapidly changing slopes. J. Fluid Mech. 833, 70–97.
Nogueira, H.I., Adduce, C., Alves, E., Franca, M.J., 2013. Analysis of lock-exchange gravity currents over smooth and rough beds. J. Hydraul. Res. 51 (4), 417–431.
Nogueira, H.I., Adduce, C., Alves, E., Franca, M.J., 2014. Dynamics of the head of gravity currents. Environ. Fluid Mech. 14, 519–540.
Ooi, S.K., Constantinescu, G., Weber, L., 2009. Numerical simulations of lock-exchange compositional gravity current. J. Fluid Mech. 635, 361–388.
Ottolenghi, L., Adduce, C., Roman, F., Armenio, V., 2017. Analysis of the flow in gravity currents propagating up a slope. Ocean. Model. 115, 1–13.
Ottolenghi, L., Prestininzi, P., Montessori, A., Adduce, C., La Rocca, M., 2018. Lattice Boltzmann simulations of gravity currents. Eur. J. Mech. B Fluids 67, 125–136.
Pang, B., Ding, Y., Wang, Y., 2023. Flow behavior analysis in boundary layer transition based on the Liutex–shear decomposition. AIP Adv. 13 (2).
Pham, H.T., Sarkar, S., Brucker, K.A., 2009. Dynamics of a stratified shear layer above a region of uniform stratification. J. Fluid Mech. 630, 191–223.
Shin, J., Dalziel, S., Linden, P., 2004. Gravity currents produced by lock exchange. J. Fluid Mech. 521, 1–34.
Shrestha, P., Nottage, C., Yu, Y., Alvarez, O., Liu, C., 2021. Stretching and shearing contamination analysis for liutex and other vortex identification methods. Adv. Aerodyn. 3, 1–20.
Simpson, J.E., 1999. Gravity Currents: In the Environment and the Laboratory. Cambridge University Press.
Tanino, Y., Nepf, H., Kulis, P., 2005. Gravity currents in aquatic canopies. Water Resour. Res. 41 (12).
Testik, F., Ungarish, M., 2016. On the self-similar propagation of gravity currents through an array of emergent vegetation-like obstacles. Phys. Fluids 28 (5).
Theodorsen, T., 1955. The structure of turbulence. In: 50 Jahre Grenzschichtforschung: Eine Festschrift in Originalbeiträgen. Springer, pp. 55–62.
Tian, S., Gao, Y., Dong, X., Liu, C., 2018. Definitions of vortex vector and vortex. J. Fluid Mech. 849, 312–339.
Tokyay, T., Constantinescu, G., Gonzalez-Juez, E., Meiburg, E., 2011. Gravity currents propagating over periodic arrays of blunt obstacles: Effect of the obstacle size. J. Fluids Struct. 27 (5–6), 798–806.
Wiliamson, C., 1996. Vortex dynamics in the cylinder wake.
Xia, Y., 2021. Liutex in vortex statistics of 2D turbulent system. In: Liutex and Third Generation of Vortex Definition and Identification: An Invited Workshop from Chaos 2020. Springer, pp. 215–225.
Xu, W., Gao, Y., Deng, Y., Liu, J., Liu, C., 2019. An explicit expression for the calculation of the rortex vector. Phys. Fluids 31 (9).
Xu, W.q., Wang, Y.q., Gao, Y.s., Liu, J.m., Dou, H.s., Liu, C., 2019. Liutex similarity in turbulent boundary layer. J. Hydrodyn. 31, 1259–1262.
Zhan, J.m., Li, Y.t., Wai, W.h.O., Hu, W.q., 2019. Comparison between the Q criterion and rortex in the application of an in-stream structure. Phys. Fluids 31 (12).
Zhang, X., Nepf, H.M., 2008. Density-driven exchange flow between open water and an aquatic canopy. Water Resour. Res. 44 (8).
Zhang, W., Zapata, M.U., Bai, X., Pham-Van-Bang, D., Nguyen, K.D., 2020. Three-dimensional simulation of horseshoe vortex and local scour around a vertical cylinder using an unstructured finite-volume technique. Int. J. Sediment Res. 35 (3), 295–306.
Zhou, J., Adrian, R.J., Balachandar, S., Kendall, T., 1999. Mechanisms for generating coherent packets of hairpin vortices in channel flow. J. Fluid Mech. 387, 353–396.
Zhou, J., Venayagamoorthy, S.K., 2020. How does three-dimensional canopy geometry affect the front propagation of a gravity current? Phys. Fluids 32 (9).
Zhu, D.Z., Lawrence, G.A., 2001. Holmboe's instability in exchange flows. J. Fluid Mech. 429, 391–409.
Zhu, J.B., Lee, C.B., Chen, G.Q., Lee, J.H.W., 2006. PIV observation of instantaneous velocity structure of lock release gravity currents in the slumping phase. Commun. Nonlinear Sci. Numer. Simul. 11 (2), 262–270.
Zordan, J., Juez, C., Schleiss, A.J., Franca, M.J., 2018a. Entrainment, transport and deposition of sediment by saline gravity currents. Adv. Water Resour. 115, 17–32.
Zordan, J., Schleiss, A., Franca, M., 2018b. Structure of a dense release produced by varying initial conditions. Environ. Fluid Mech. 18 (5), 1101–1119.